Chinese Journal of Aeronautics, (2025), 38(7): 103461

Chinese Society of Aeronautics and Astronautics
& Beihang University

Chinese Journal of Aeronautics

cja@buaa.edu.cn
www.sciencedirect.com

FULL LENGTH ARTICLE

Optimal disturbances and growth patterns in hypersonic blunt-wedge flow

Yifeng CHEN [a], Tianju MA [b], Peixu GUO [a,*], Jiaao HAO [a], Chihyung WEN [a]

[a] *Department of Aeronautical and Aviation Engineering, The Hong Kong Polytechnic University, Hong Kong SAR 999077, China*
[b] *Academy of Aerospace Propulsion Technology, Xi'an 710100, China*

Received 29 May 2024; revised 25 July 2024; accepted 9 August 2024
Available online 5 March 2025

KEYWORDS

Hypersonic flow;
Boundary layer stability;
Resolvent analysis;
Optimal disturbance;
Blunt body

Abstract In hypersonic boundary layers, the optimal disturbance is notably caused by normal-mode instabilities, such as Mack second mode. However, recent experimental and numerical efforts have demonstrated the dominance of nonmodal growth in hypersonic flows with the presence of moderate nose bluntness. In this study, resolvent analysis and parabolized stability equation analysis are performed to investigate the instabilities over a blunt-tip wedge. Main parameters include Mach number 5.9, unit Reynolds number 91.5×10^6/m, half wedge angle 5°, and nose radii ranging from 2.54 mm to 15.24 mm. Two novel growth patterns of travelling waves are identified to compete, whose nature is the intersection of the energy gain of optimal and sub-optimal disturbances. Pattern A with large spanwise wavelengths has the signature of slow energy amplification over a long distance which concentrates in the entropy layer. By contrast, pattern B with relatively small spanwise wavelengths presents rapid transient growth inside the boundary layer. A systematic study is performed on the growth/attenuation mechanism of disturbance patterns and the effects of wall temperature and nose radius. Wall cooling is found to be an alternative control strategy aimed at nonmodal instabilities. The receptivity to slow acoustic waves is considered when the effect of bluntness is studied. An estimated amplitude response favorably reproduces the reversal-like phenomenon. The lift-up/Orr mechanism analysis provides an explanation of energy growth for nonmodal responses.

1. Introduction

The prediction and control of laminar-turbulent transition of boundary layers are long-standing challenges for the design of hypersonic vehicles. The transition can result in an abrupt increase of skin friction and heat flux and thereby impair the performance of hypersonic vehicles.[1] Therefore, accurate transition prediction and effective control of the transition onset are of great importance. In a realistic flight environment, the

* Corresponding author.
E-mail address: peixu.guo@outlook.com (P. GUO).
Peer review under responsibility of Editorial Committee of CJA

https://doi.org/10.1016/j.cja.2025.103461

freestream disturbances are usually of low amplitude, under which the transition over configurations with a sharp leading edge tends to be due to the exponential growth of unstable normal modes inside the boundary layers. Common normal modes usually include the Tollmien–Schlichting mode, the first mode, and the second mode for low-speed, supersonic, and hypersonic boundary layers, respectively.[2–4] Generally, the leading edge of high-speed vehicles can be artificially blunted to reduce the nose heat transfer. The bluntness would give rise to a detached bow shock and an entropy layer with a strong entropy gradient consequently. The entropy layer reduces the local Reynolds number at the boundary-layer edge and stabilizes the boundary layer.[5,6] The appearance of the entropy layer may also affect the transition mechanism of the boundary layer. As reported by the hypersonic wind-tunnel experiment,[7] the transition onset would first move downstream with the increment of the nose radius, and then upstream when the nose radius exceeds a threshold value. This phenomenon is called the 'transition reversal'. The downstream movement of the transition onset qualitatively agrees with the result of stability analysis,[8,9] which shows that the second mode is highly stabilized as the nose radius increases.[7,10] Moreover, the newly generated instability, i.e., the entropy layer mode with the appearance of bow shock has been reported to be insignificant in triggering the transition due to its low growth rate and narrow growth region near the leading edge.[6,11–14]

Despite the fact that the 'transition reversal' phenomenon was first reported 40 years ago,[7] the reason behind it remains a debate. Recently, the nonmodal growth has been considered potentially responsible for the transition reversal, where the modal disturbances are relatively weak to trigger the transition at the experimental onset location.[15,16] According to the resolvent analysis and direct numerical simulation conducted by Paredes et al., [15,17–20] the nonmodal disturbance inside the entropy layer can further penetrate the boundary layer and eventually cause the transition. Hartman et al.[21] investigated the nonlinear breakdown process on a blunt cone. It is indicated that when the linear unstable oblique waves initiated in the entropy layer possessed an appropriate initial amplitude, they would lead to a rapid transition before the instability region of the second mode. Moreover, schlieren images of the inclined structure signature of nonmodal disturbances were reported by the experiment of Kennedy et al.,[22,23] which highlighted the critical role of nonmodal instabilities. More recent research of instabilities over Ogive-Cylinder models[24–26] reported three disturbance patterns: rope-like, elongated, and wisp-like structure disturbances corresponding to the second mode, the first mode, and the disturbance inside the entropy layer, respectively, accompanying with the increase of nose bluntness. However, with the perturbation imposed downstream of the bow shock, direct numerical simulation presented a monotonous delay of the transition onset as bluntness was increased. In contrast, considering the freestream receptivity process by introducing forcings upstream of the bow shock, the importance of non-Mack-mode disturbances was also reported in hypersonic flow over blunt flat plates beyond the critical reversal nose radius.[27] The unstable first or second mode is generated by a resonance process due to the synchronization of the phase speed of discrete modes.[3] In general, the first and second modes correspond to signals with physical frequencies of tens and hundreds of kilohertz, respectively. In hypersonic flows over increasingly blunted models, the most energetic disturbance presents a shift from high-frequency bands toward low-frequency ones,[15,24] which might imply the significance of the first-mode or nonmodal instabilities.[24] In the noisy wind-tunnel conditions, the disturbance in the incoming freestream is dominated by the slow acoustic wave,[28] which has been identified in wind-tunnel experiments[29–32] and widely recognized in numerical simulations[3,4,33] and applied in improved transition prediction methods.[34,35] The acoustic wave originates mostly from the acoustic radiation of the nozzle-wall turbulent boundary layer. Thus the receptivity to the slow acoustic wave is considered when investigating the bluntness effect.

Despite the above reviews regarding the significant role of nonmodal disturbances, the distribution patterns of different optimal disturbances (streaks, oblique waves, and planar waves) and their dependence on external factors, such as wall temperature and bluntness, remain scarcely discussed and poorly understood. The appearance of the most amplified disturbances in either the entropy layer or the boundary layer eventually results in different physical mechanisms of transition to turbulence. The information about the wall-normal locations of optimal disturbances would benefit the proposal of possible control techniques as well. Therefore, it is fundamentally crucial to determine in which region the most energetic disturbance undergoes energy amplification. In this paper, a resolvent analysis of a blunt wedge flow is performed to reveal the strongest response to external forcings. In the linear instability stage, the resolvent analysis has been proven by the authors to have an equal accuracy as the direct numerical simulation.[36] Meanwhile, a modal Parabolized Stability Equation (PSE) analysis is employed to reveal the region of normal-mode instabilities. The classical Orr and lift-up nonmodal growth mechanisms will be examined to interpret how the nonmodal instabilities are amplified in the entropy/boundary layer.

Another noteworthy issue is the control of nonmodal disturbances over such blunted models. Wall manipulations, such as acoustic metasurfaces implemented by porous coatings, have been confirmed by the authors to effectively suppress the second-mode instability.[36–39] As for the wall cooling effect, its suppression on the first mode and destabilizion on the second mode have been illustrated both in early stability analysis[40–42] and recent energy source analysis.[43] It is found that wall cooling stabilizes the first mode by weakening the Reynolds thermal stress and dilatation fluctuations. Meanwhile, wall cooling destabilizes the second mode by producing a new, active zone of wall-normal internal energy transport beneath the second generalized inflection point. The effects of local heating and cooling on the nonlinear and breakdown stages are systematically reported by Zhou et al.[44] For control strategies for crossflow mode induced by generalized inflection point of spanwise profiles, Nie et al.[45] indicated that a flat pressure distribution and a short leading-edge flow acceleration zone are beneficial for controlling cross-flow instabilities. However, to the best knowledge of the authors, rare attention has been paid to controlling the nonmodal instability over moderately or largely blunted models. Obviously, it is of engineering significance to control the dominant nonmodal instabilities over blunt bodies. A relevant and inspiring study by Tempelmann et al.[46] on swept plate models suggested that wall cooling could stabilize crossflow modes while destabilizing disturbances of nonmodal nature. Regarding transient growth in

compressible boundary-layer flows, the wall temperature effect was studied on the optimal disturbances over a flat plate[47] and a sphere.[48] The literatures reported that wall cooling could destabilize the low-Mach-number boundary layer. Nevertheless, a detailed energy analysis from the transient growth mechanism is lacking and necessary. The eligibility of the wall cooling strategy merits further considerations for nonmodal instabilities over the blunt wedge, and the control mechanism needs to be comprehended. Currently, it is well-recognized that wall cooling would stabilize the first mode. The energy analysis of our previous work[43] indicated that the stabilization mechanism is highly related to the mean shear reduction. In terms of the concerned nonmodal disturbances, the dominant component appears to be the temperature perturbation.[16] Therefore, it will be of further interest in this paper to evaluate the effect of wall cooling or heating as a potential controlling technique for nonmodal instabilities over blunt bodies.

This paper is intended to deepen the understanding of the characteristics of modal and nonmodal instabilities in hypersonic flows over blunt bodies. It is expected to throw light on the effects of wall temperature, nose radius, and the underpinning transient growth mechanism. The resolvent analysis, parabolized stability equation, and direct numerical simulation are employed. The optimal responses inside the entropy layer or boundary layer are systematically examined. As for the effect of bluntness, only receptivity and linear growth stages are investigated and discussed, while nonlinear interaction and transitional stages will be studied in the future. This paper is organized as follows: Section 2 provides the investigated model, the parametric setup, and the numerical methods for base flow calculation and stability analysis. Section 3 shows the results and discussions, which are divided into 5 parts. The base flow over the blunt wedge is presented in Section 3.1. The distribution patterns of the optimal responses with different frequencies and spanwise wavenumbers are depicted in Section 3.2. Subsequently, the effects of wall cooling and bluntness are examined in Sections 3.3 and 3.4, respectively. The Orr and lift-up mechanisms are explored from the perspective of energy and vorticity evolutions in Section 3.5. Finally, the main findings are summarized in Section 4. In particular, the appendix section provides an example for understanding the competition among different types of disturbances, which are manifested as the optimal response and a series of suboptimal disturbances.

2. Model, flow condition and analysis tool

2.1. Geometric configuration and flow conditions

The freestream flow condition investigated here follows that by Paredes et al.[16] at Mach number 5.9 and a unit Reynolds number of 91.5×10^6/m. The freestream static and total temperatures are 76.74 K and 611 K, respectively. The baseline wall temperature is 300 K with $T_w/T_{ad} = 0.57$, where the subscripts w and ad refer to quantities at the wall and under the adiabatic wall condition, respectively. Here, T_{ad} is the laminar recovery temperature. The studied model is a blunt wedge with a 5° half-wedge angle. Three nose radii (R_n*) are studied, including 2.54 mm, 5.08 mm, and 15.24 mm. The asterisk represents dimensional quantities. Based on the experimental data,[16,49] the reversal Reynolds number based on the nose radius is around 1×10^6 for the cone. Thus, the radii 2.54 mm and 15.24 mm can be regarded as moderate and large blunted cases, respectively. The grid independence is verified and shown in Appendix A, which demonstrates the results of both the base flow and resolvent analysis are converged under the considered grid resolution.

2.2. Computational methods

The computational and theoretical approaches are similar to the framework in our previous publication. [50] The same numerical codes are adopted. It seems unavoidable that numerics for baseflow calculation, resolvent analysis, normal-mode stability analysis, the definition of energy norm, etc. look similar. The unchanged methodology has been found to be reliable in reaching the research objective. The governing equation for the calculation of base flow is the compressible Navier-Stokes equation in a conservation form:

$$\frac{\partial \boldsymbol{U}}{\partial t}+\frac{\partial \boldsymbol{F}}{\partial x}+\frac{\partial \boldsymbol{G}}{\partial y}+\frac{\partial \boldsymbol{H}}{\partial z}=\boldsymbol{0} \tag{1}$$

where $\boldsymbol{U} = [\rho, \rho u, \rho v, \rho w, \rho e]^{\mathrm{T}}$ is the vector of conservative variables, the superscript "T" denotes the transpose, and $\boldsymbol{F}$, $\boldsymbol{G}$, and $\boldsymbol{H}$ are vectors of fluxes. Here, ρ represents density, and u, v, and w are the velocities in the x, y, and z directions, which denote streamwise, wall-normal, and spanwise directions, respectively. Meanwhile, a body-fitted orthogonal coordinate system is constructed, which is represented by (ξ, η, z). Total energy per unit mass is denoted by e. The perfect gas model is employed with a constant specific heat ratio of 1.4. Besides, the dynamic viscosity is calculated using Sutherland's law, and the thermal conductivity coefficient is calculated based on a constant Prandtl number 0.72. The freestream variables are utilized for non-dimentionalization except that the pressure is by $\rho_\infty^* u_\infty^* u_\infty^*$ (the subscript ∞ represents freestream quantities), and the reference length is set to 1 mm.

In general, the steady base flow is first calculated, and subsequently the resolvent and Parabolized Stability Equation (PSE) analyses are performed based on the converged base flow. For a time-stationary flow, the vector of conservative variables can be decomposed into the base-flow and perturbation parts:

$$\boldsymbol{U}(x,y,z,t) = \bar{\boldsymbol{U}}(x,y) + \boldsymbol{U}'(x,y,z,t) \tag{2}$$

where the overbar ¯ and prime ′ represent base-flow and perturbed variables, respectively.

2.2.1. Base flow and slow acoustic wave model

The base flow is calculated using an in-house multi-block parallel finite-volume solver called PHAROS, which has been successfully employed in various configurations, such as the compression corner, the double wedge, and the double cone models. [51–53] The inviscid flux is calculated by MUSCL scheme and a modified Steger-Warming scheme, and the second-order central difference scheme is utilized for viscous flux discretization. Pseudo-time advancing is achieved by the implicit line relaxation method. More detailed information for the PHAROS can be found in the Ref. 53. In terms of the boundary condition, the $y = 0$ boundary of the computational domain is set to be symmetric, the upper boundary is farfield, the right boundary is outflow via extrapolation, and the wall

boundary is no-slip and isothermal or adiabatic, depending on the case.

To explore the effect of nose bluntness (Section 3.4), the receptivity process to free stream slow acoustic waves is considered. The slow acoustic wave is added to the freestream boundary of the computational domain. The dimensionless fluctuation of the plane slow acoustic wave is[13]

$$\begin{bmatrix} \rho' \\ u' \\ v' \\ p' \end{bmatrix} = \begin{bmatrix} A_\infty Ma_\infty^2 \\ -A_\infty Ma_\infty^2 \\ 0 \\ A_\infty \end{bmatrix} e^{i(\alpha x-\omega t)} + \text{c.c.} \tag{3}$$

where A_∞ is the small amplitude of the freestream disturbance, ω is the angular frequency, α is the streamwise wavenumber, and c.c. denotes complex conjugate. In this study, the incident angle of the slow acoustic wave is set to zero and the dispersion relation of is $\alpha = \omega/(1-1/Ma_\infty)$. In the simulation of the receptivity process, the three-stage third-order Runge-Kutta method is employed for time advancement.

2.2.2. Resolvent analysis for optimal disturbance

Substituting Eq. (2) into Eq. (1) and neglecting non-linear high order terms yield the linearized Navier-Stokes equation:

$$\frac{\partial \boldsymbol{U}'}{\partial t} + \frac{\partial \boldsymbol{F}'}{\partial x} + \frac{\partial \boldsymbol{G}'}{\partial y} + \frac{\partial \boldsymbol{H}'}{\partial z} = \boldsymbol{0} \tag{4}$$

To examine the response to external forcings, consider a small amplitude forcing term $\boldsymbol{f}'$ added to the right-hand side of Eq. (4). Reformulating the governing equation, we obtain

$$\frac{\partial \boldsymbol{U}'}{\partial t} = \boldsymbol{A}\boldsymbol{U}' + \boldsymbol{B}\boldsymbol{f}' \tag{5}$$

where $\boldsymbol{A}$ is the Jacobian matrix related to the base-flow variables, and matrix $\boldsymbol{B}$ constrains the forcing to be added at a certain location $x = x_0$. The value of x_0 is 20, except in Section 3.4 (where $x_0 = 40$) to avoid the effect of the bow shock. In this study, the localized forcing is imposed to excite response from upstream regions, and thus it is of interest to observe how the disturbances of convective-instability nature are propagated downstream and amplified or attenuated. Thus, a constrained optimization problem will be solved without modifying the Jacobian matrix $\boldsymbol{A}$, which has been applied in our previous works.[50,51,54] The harmonic assumption is made for a small-amplitude perturbation vector $\boldsymbol{U}'$

$$\boldsymbol{U}'(x,y,z,t) = \hat{\boldsymbol{U}}(x,y)\exp(i\beta z - i\omega t) + \text{c.c.} \tag{6}$$

where $\hat{\boldsymbol{U}}$ is the complex eigenfunction, β is the spanwise wavenumber. Similarly, the harmonic forcing can be written as

$$\boldsymbol{f}'(x,y,z,t) = \hat{\boldsymbol{f}}(x,y)\exp(i\beta z - i\omega t) + \text{c.c.} \tag{7}$$

Substituting Eqs. (6) and (7) into Eq. (5) gives

$$\begin{cases} \hat{\boldsymbol{U}} = \boldsymbol{R}\boldsymbol{B}\hat{\boldsymbol{f}} \\ \boldsymbol{R} = (-i\omega\boldsymbol{I} - \boldsymbol{A})^{-1} \end{cases} \tag{8}$$

which indicates the relationship between the external forcing and the linear response of the system. Here, the identity operator is represented by $\boldsymbol{I}$.

In the resolvent analysis, the maximal amplification of the energy, i.e. the optimal gain σ^2, is targeted. The optimal gain is defined in the parametric space (β, ω) by the energy ratio between the output responses and the input forcings:

$$\sigma^2(\beta,\omega) = \max_{\hat{f}} \frac{\| \hat{\boldsymbol{U}} \|_E}{\| \boldsymbol{B}\hat{\boldsymbol{f}} \|_E} \tag{9}$$

Here, Chu's energy[55] is utilized for the calculation of the energy norm as

$$\| \hat{\boldsymbol{U}} \|_E = \int_\Omega \boldsymbol{U}^\dagger \boldsymbol{M} \hat{\boldsymbol{U}} \mathrm{d}x\mathrm{d}y \tag{10}$$

where Ω represents the computational domain for resolvent analysis, the superscript † refers to the conjugate transpose, and $\boldsymbol{M}$ is the weight operator given by Bugeat et al.[56] The dimensionless expression of Chu's energy at a local station is given by

$$E_{\text{Chu}}(x) = \frac{1}{2}\int_0^\infty \left[\bar{\rho}(u'^2 + v'^2 + w'^2) + \frac{\bar{T}}{\gamma Ma_\infty^2 \bar{\rho}}\rho'^2 + \frac{\bar{\rho}}{\gamma(\gamma-1)Ma_\infty^2 \bar{T}}T'^2 \right] \mathrm{d}y \tag{11}$$

The three terms on the right-hand side of Eq. (10) denote fluctuations of kinetic energy, potential energy, and internal energy, respectively. The computer code utilized for resolvent analysis here has been well validated by our previous works and detailed in Refs. 50,51.

2.2.3. Stability analysis

To examine the normal-modal instability feature of the optimal response, Linear Stability Theory (LST) and PSE analyses are performed. Specifically, LST provides the initial eigenfunction profiles to PSE for spatial marching, which gives the evolution of the modal instability. In PSE, the disturbance $\boldsymbol{\psi}'$ is expressed by

$$\boldsymbol{\psi}'(x,y,z,t) = \hat{\boldsymbol{\psi}}(x,y)\exp\left(i\int_{x_0}^{x}\alpha' \mathrm{d}\tilde{x} + i\beta z - i\omega t\right) \tag{12}$$

where the vector $\boldsymbol{\psi} = [\rho, u, v, w, T]^{\mathrm{T}}$, $\hat{\psi}$ and α' are the shape function and the complex streamwise wavenumber, respectively, and x_0 is the initialization location of PSE marching.

Substituting Eq. (12) into Eq. (4) gives rise to the PSE as [50]

$$(\boldsymbol{\Gamma}_0 + \boldsymbol{\Gamma}_1)\hat{\boldsymbol{\psi}} + \boldsymbol{\Gamma}_2\frac{\partial \hat{\boldsymbol{\psi}}}{\partial x} + \frac{\partial \alpha}{\partial x}\boldsymbol{\Gamma}_3\hat{\boldsymbol{\psi}} = \boldsymbol{0} \tag{13}$$

The effects of the locally parallel flow, the non-parallel base flow, the non-local shape function, and the streamwise-varying wavenumber are absorbed in the base-flow-related operators $\boldsymbol{\Gamma}_0$, $\boldsymbol{\Gamma}_1$, $\boldsymbol{\Gamma}_2$, and $\boldsymbol{\Gamma}_3$, respectively. An eigenvalue problem is solved in LST when keeping only the local operator $\boldsymbol{\Gamma}_0$ in Eq. (12). In this study, PSE is initialized by mode S, which may evolve into the unstable first mode downstream, depending on the flow parameters such as the input frequency.[4] The calculation is performed by our in-house code CHASES, which has been validated compared with both theoretical [57–59] and DNS [50,51,54] results. The details of numerical methods can be found in these references.

3. Presentation of results

In this section, the results of the numerical simulation and stability analysis will be presented and discussed. The base flows for the considered three nose radii are shown in Section 3.1. The characteristics of different optimal disturbances will be

focused on in Section 3.2 for a moderate bluntness $R_n^* = 2.54$-mm with $T_w/T_{ad} = 0.57$. Following that, the effects of wall temperature and bluntness will be examined in Sections 3.3 and 3.4, respectively. Finally, the transient growth mechanism will be analyzed in Section 3.5.

3.1. Base flow

The solid and dashed black lines mark the locations of the boundary layer edge and the entropy layer edge, respectively.

The contours of the Mach number for cases with different nose radii are shown in Fig. 1 with $T_w/T_{ad} = 0.57$. The criterion to determine the boundary layer edge is set to the location where $h_t/h_{t,\infty} = 0.995$, where h_t is the total enthalpy. The entropy-layer edge is defined as the wall-normal location where the entropy increment equals 0.25 times the entropy increment at the local wall. The entropy increment is defined as

$$\Delta S^* = c_p^* \ln\left(\bar{T}^*/\bar{T}_\infty^*\right) - R^* \ln\left(\bar{p}^*/\bar{p}_\infty^*\right) \tag{14}$$

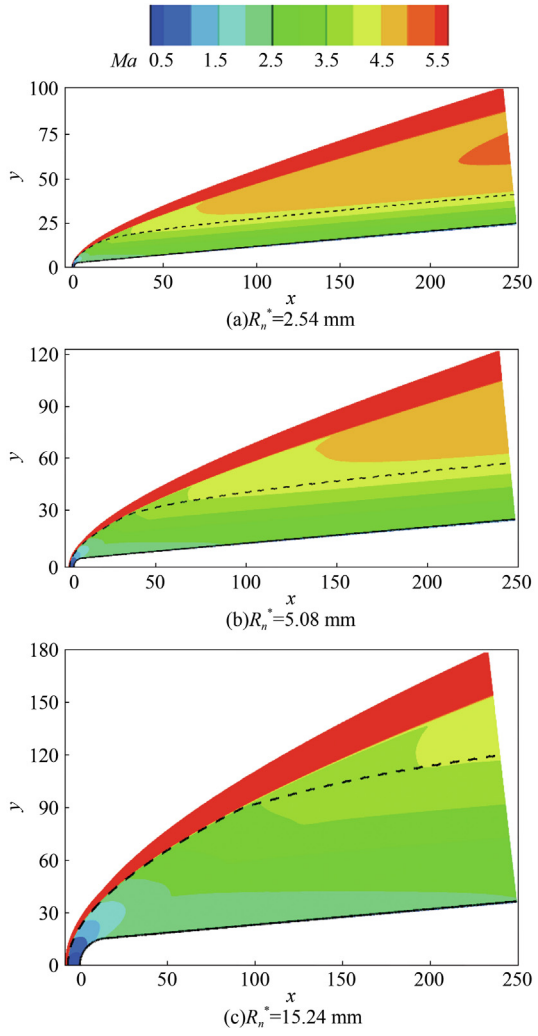

Fig. 1 Contours of Mach number for blunt wedges. The solid and dashed black lines mark the locations of the boundary layer edge and the entropy layer edge, respectively.

where c_p^* is the specific heat at constant pressure, and R^* is the specific gas constant. The entropy-layer effect over a wedge[60] is stronger than that over a cone[13] under the same freestream conditions, as the streamline keeps nearly parallel to the wall downstream.[61] As shown in Fig. 1, as the nose radius is increased, the entropy layer region is enlarged. According to the stability analysis,[8] the first/second mode usually appears downstream, and the entropy-layer mode emerges upstream. The latter has a relatively low growth rate, which is not likely to dominate the transition process.[60] On the other hand, the enhanced entropy layer may have an effect on the nonmodal disturbance generated herein. The effect of bluntness on the optimal disturbance will be discussed in Section 3.4.

3.2. Features of optimal disturbances

After the converged base flow is obtained, the resolvent analysis is performed. The characteristics of the optimal responses, including streaks, plane, and oblique traveling disturbance, will be discussed in this section.

Fig. 2 shows the plots of the optimal gain for different frequencies and spanwise wavenumbers and the N-factor distributions along the x direction for typical optimal oblique disturbances and plane waves. The N-factor is defined by $N = 0.5\ln(E_{\mathrm{Chu}}/E_{\mathrm{Chu},0})$, where $E_{\mathrm{Chu},0}$ is measured at $x = x_0$ and N is set to be 0 at x_0. For brevity, (0.3, 0) represents the optimal response for a Fourier mode with $\omega = 0.3$ and $\beta = 0$, and similarly for other optimal disturbances. Generally, in Fig. 2(a), the maximum energy gain exhibits a monotonous decreasing trend as the frequency is increased. An interesting finding is that as β increases, the optimal response switches from pattern A (open symbols) to pattern B (solid symbols). The former pattern is mainly distributed inside the entropy layer between the entropy-layer edge and boundary-layer edge, while the latter shows its signature inside the boundary layer. As shown in Fig. 2(b), the N-factor of the pattern-A response (including plane waves and oblique waves when β is relatively small) grows at a moderate rate till the end of the computational domain. In contrast, pattern-B responses with large β undergo a rapid transient growth immediately downstream of the forcing location, followed by a decay process. Note that the pattern-B waves were not identified in some similar studies on the optimal disturbances such as by Paredes et al. [16] This is probably due to the different definitions of the energy gain. Paredes et al. [16] used the ratio of energy at two different streamwise locations as the optimization object function, whereas the present work considers the energy integrated over the whole domain (see Eqs. (9), (10)). The former definition may miss the possible energy overshoot, which was also realized by Paredes et al.[15] The energy overshoot may occur over configurations such as hypersonic blunt forebodies, [19] which are manifested as pattern-B waves in this paper. In this study, the optimal response pattern A and pattern B, are the products obtained from a selection process. In detail, the maximum energy gain is sought for different β at a fixed frequency. Two different patterns exactly appear in the respective entropy and boundary layers, corresponding to small- and large-wavenumber responses, respectively. The natural external disturbance is a combination of broadband frequencies and various wavenumbers in wind tunnels.[62] In realistic conditions, these patterns usually coexist subject to broadband incoming

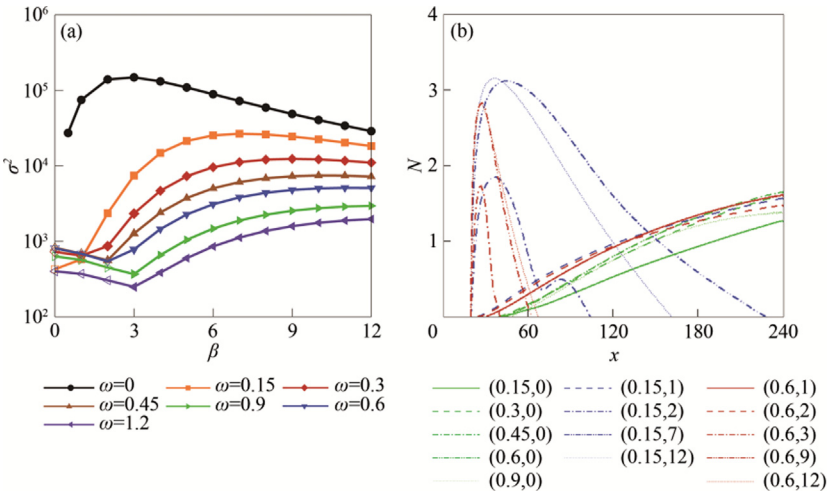

Fig. 2 (a) Optimal gains for different frequencies and spanwise wavenumbers (open symbols represent pattern A and solid symbols represent pattern B), and (b) N-factor distributions for typical optimal disturbances along x direction.

disturbances. They can be distributed in different regions (boundary layer and entropy layer).

The turning of the gain curve in Fig. 2(a) as the state transitions from pattern A to pattern B may indicate a competition of different growth patterns. To confirm this deduction, the Arnoldi iteration method is further employed in the resolvent analysis to find a series of sub-optimal disturbances. An illustration of the competitive physical image between different growth patterns is shown in the Appendix B. The turning point of the optimal gain curve in Fig. 2(a) is actually the intersection of the gain between optimal and the first sub-optimal responses. For brevity, only the optimal response is discussed in the main body.

When the nose bluntness exceeds a threshold, modal instabilities tend to be too weak to trigger the transition, and transient growth of low-frequency disturbances is of particular significance.[15] Therefore, for blunt wedges with moderate or large nose radius, high-frequency disturbances are less considered. In fact, no pronounced second-mode instabilities are observed in the case considered here. In the following analysis, three kinds of representative forcings and associated optimal responses of the system, i.e., streaks, planar waves, and oblique waves, will be presented and discussed. The contributions of different parts of energy are quantified based on Chu's energy. For example, the contribution of the streamwise velocity fluctuation is evaluated by the indicator I_u

$$I_u(x) = \int_0^\infty \left(\bar{\rho}\,\overline{u'^2}\right) \mathrm{d}y / 2E_{\mathrm{Chu}} \tag{15}$$

Similar indicators can be obtained for the fluctuations of the wall-normal velocity, the spanwise velocity and thermodynamic quantities.

Fig. 3 provides contours of streamwise temperature and velocity fluctuations of streaks (0, 2), which are mainly distributed inside the boundary layer. The input eigenfunction profiles and I indicators of Chu energy for streak (0, 2) are shown in Fig. 4. It is found that the main component of the forcing is constituted by the spanwise forcing. In terms of the downstream response, the streamwise velocity fluctuation (I_u) grows rapidly as it evolves downstream. A marginal contribution comes from the temperature and density fluctuations. The transfer of the dominant component indicates a classical lift-up mechanism, which will be discussed in detail in Section 3.5.

As shown in Fig. 5, the evolution of the plane wave (0.45, 0) shows a different signature from that of the streaks, which is a representative pattern-A response and is mainly distributed inside the entropy layer. Similar growth patterns can be obtained for the optimal response when β is small, such as (0.6, 1) and (0.6, 2), as indicated by the N-factor in Fig. 2(b). The prominent role of disturbance inside the entropy layer for moderately blunt models was also reported in the experiments for ogive-cylinder[25] and blunt cones.[22] However, as mentioned above, the blunt wedge configuration encounters a stronger entropy layer, and the entropy swallowing phenomenon present in the cone model moves downstream in the wedge model.[61] This difference may delay the disturbance evolution inside the entropy layer to penetrate the boundary and, in turn, affect the transition process. Fig. 6 plots the input eigenfunction profiles and I indicators of Chu energy for the plane wave (0.45, 0). The forcing component in the streamwise velocity equation constitutes the main component of the input forcings. The streamwise velocity response experiences a gradual decay downstream, while the internal energy components (temperature and density fluctuation) continue to grow and become dominant. Meanwhile, the tilting structure may indicate the presence of the Orr mechanism, which will be discussed in detail in Section 3.5.

As for the other pattern-B response (oblique waves when β is large enough), the streamwise velocity and temperature fluctuations are mainly distributed inside the boundary layer, as shown in Fig. 7. The input forcing profiles and I indicators of Chu energy for Fourier mode (0.3, 7) are shown in Fig. 8. It appears that the distribution resembles that of the streak (0, 2), indicating a possible unsteady-streak signature for (0.3, 7). This kind of optimal response undergoes rapid growth and attenuation near the input forcing location, which has rarely been reported in previous optimal disturbance analyses on the blunt cone models.[16,20] One possibly similar observation is the disturbance reported by Hartman et al.[21] using

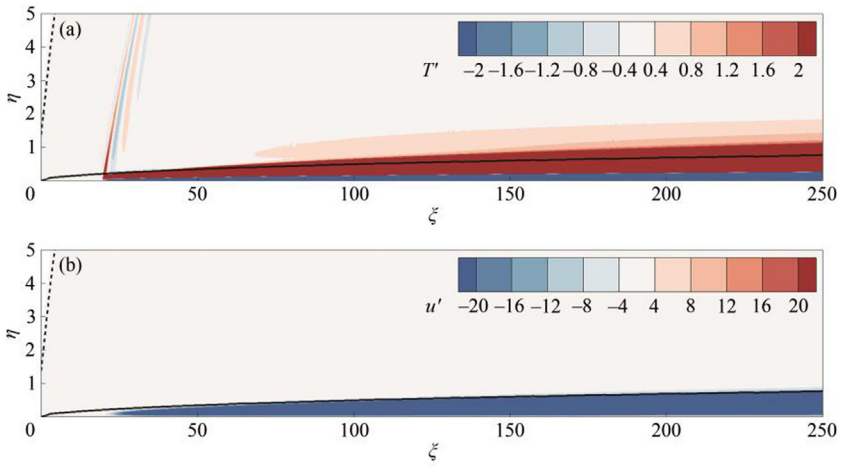

Fig. 3 Contours of normalized (a) temperature and (b) streamwise velocity perturbations of the optimal response for streaks (0, 2). The solid and dashed black lines mark the locations of the boundary layer edge and the entropy layer edge, respectively.

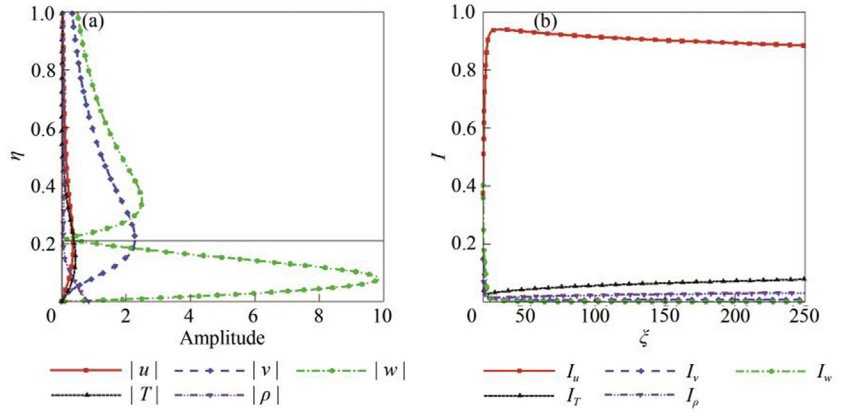

Fig. 4 (a) Input forcing profiles and (b) *I* indicators of Chu energy of optimal response for streaks (0, 2).

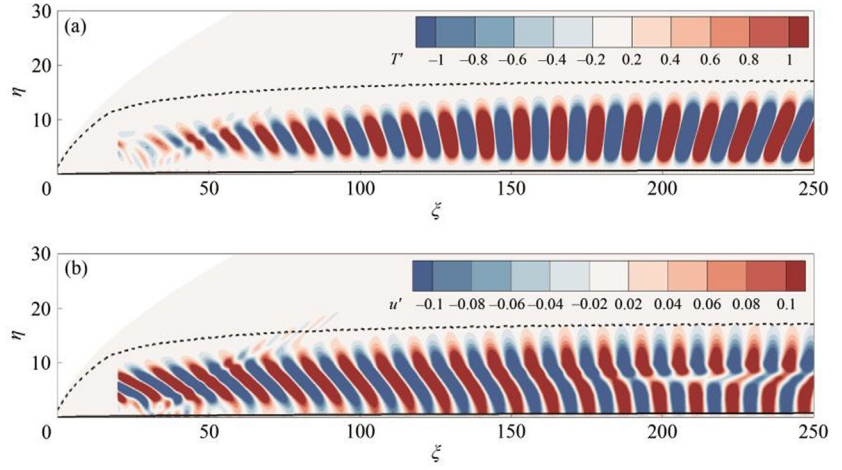

Fig. 5 Contours of normalized (a) temperature and (b) streamwise velocity perturbations of optimal response for plane wave (0.45, 0). The solid and dashed black lines mark the locations of the boundary layer edge and the entropy layer edge, respectively.

direct numerical simulation, which shows growth near the leading edge before the appearance of the second mode. The elongated structure (see Fig. 7) inside the boundary layer may indicate the occurrence of a modal instability. To clarify this point, the integrated *N*-factor is obtained by PSE that is initialized by the upstream stable mode S (normal-mode

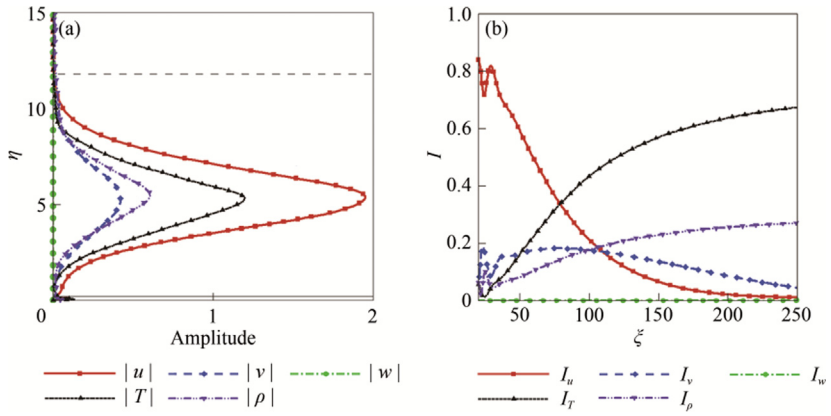

Fig. 6 (a) Input forcing profiles and (b) I indicators of Chu energy of optimal response for plane wave (0.45, 0).

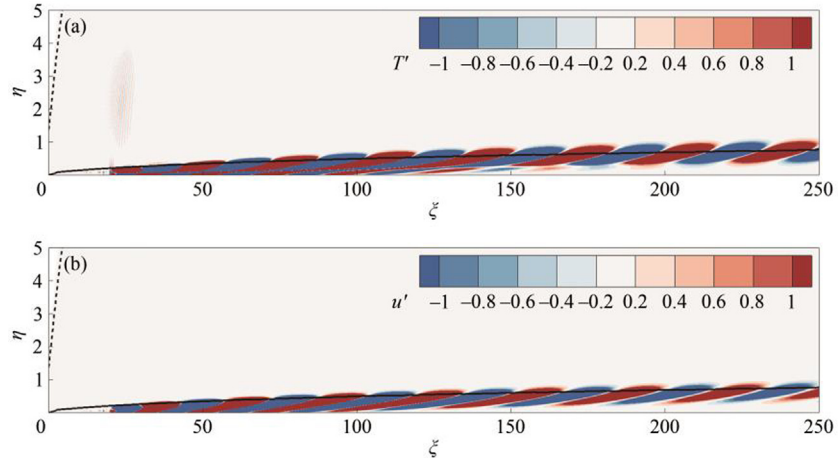

Fig. 7 Contours of normalized (a) temperature and (b) streamwise velocity perturbations of optimal response for oblique wave (0.3, 7) (pattern B). The solid and dashed black lines mark the locations of the boundary layer edge and the entropy layer edge, respectively.

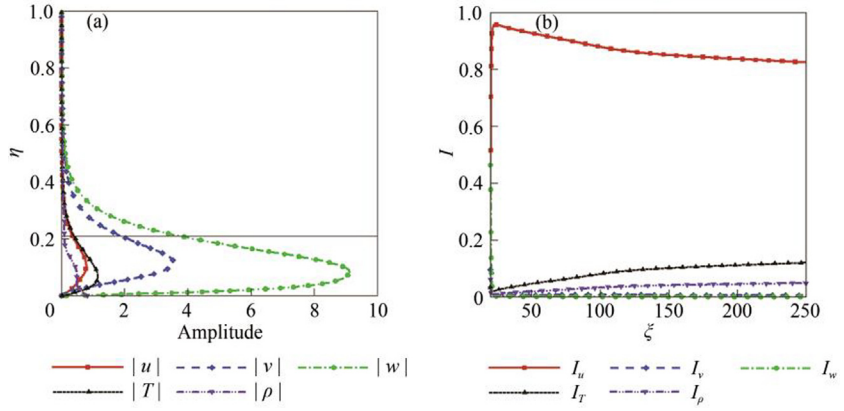

Fig. 8 (a) Input forcing profiles and (b) I indicators of Chu energy of optimal response for oblique wave (0.3, 7).

solution). The modal PSE result manifests a purely modal instability evolution. Given that the linear PSE only offers a relative growth in spatial analysis without amplitude information, the N-factor curve of PSE is shifted to match that of resolvent analysis. This operation enables a comparison of the modal evolution with respect to the curve slope, i.e., the energy growth rate. As shown in Fig. 9, a good agreement is reached for both N-factor and fluctuation profiles between resolvent analysis and PSE after an initial transient growth region when β is not large. Thus, the energy attenuation of pattern-B waves is associated with the stable normal mode.

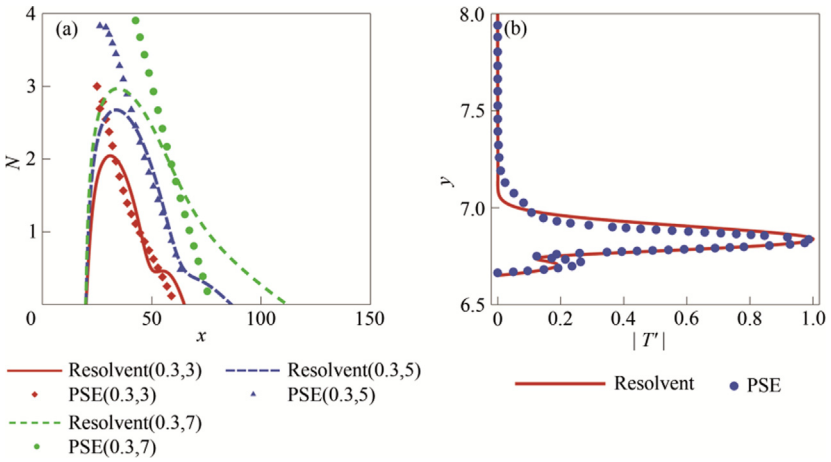

Fig. 9 Comparison of (a) integrated N factor and (b) fluctuation temperature profile for (0.3, 5) at $x = 50$ (normalized by its maximal value inside the boundary layer) obtained by PSE and resolvent analysis.

In summary, the evolution patterns of optimal streaks, plane waves, and oblique waves are studied using resolvent analysis for a moderate bluntness $R_n^* = 2.54$ mm with $T_w/T_{ad} = 0.57$. The energetic region of the resolvent response and the associated N-factor and optimal gain indicate the existence of different growth patterns. These patterns are competitive to be the most energetic one under a certain combination of ω and β, which may contribute to a competitive routine in triggering the transition. However, which routes (patterns) will finally stand out and play a dominant role in triggering the transition further depends on the receptivity process[63,64] of the disturbance in the Fourier space, as well as the nonlinear instability stage.

3.3. Effect of wall temperature

In this subsection, the adiabatic-wall case is further considered. The stabilization and destabilization effects of wall cooling on the first and second modes, respectively, have been recently explained from the perspective of energy analysis.[43] However, the effect of wall cooling on hypersonic flows where nonmodal instability is pronounced remains less understood fundamentally. As for a disturbance of nonmodal nature, wall cooling was reported to destabilize the disturbance in compressible boundary layers over swept flat plates,[46] spheres,[48] and flat plates.[47] For the present hypersonic flow over a blunt wedge, Fig. 10 shows the optimal gain for different frequencies and spanwise wavenumbers for the adiabatic wall (solid line) and baseline cold wall (dashed line) cases. Compared with the cold-wall cases, the optimal gain is generally larger under the adiabatic condition. In particular, a peak (0.15, 1) arises with a low frequency and low spanwise wavenumber, whose optimal gain exceeds those of the stationary streak, plane wave and other pattern-B oblique waves with the same frequency. Fig. 11 shows the contours of the normalized temperature and streamwise velocity perturbations for the optimal response (0.15, 1). The fluctuation is mainly distributed near the outer boundary layer, which resembles the contours of the first mode. The input forcing of the Fourier mode (0.15, 1) is shown

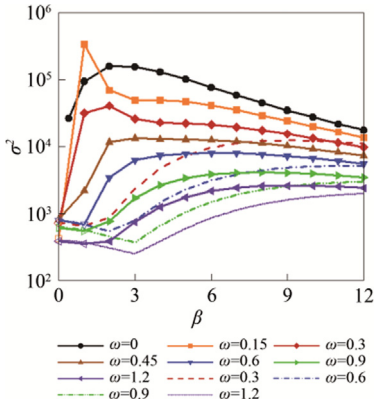

Fig. 10 Optimal gains for different frequencies and spanwise wavenumbers for $Ma = 5.9$ flow over the blunt wedge with $R_n = 2.54$ mm (solid symbols represent pattern A and hollow ones represent pattern B). Solid lines represent cases for adiabatic wall and dashed lines represent cases for $T_w/T_{ad} = 0.57$.

in Fig. 12(a). The temperature fluctuation is dominant inside the boundary layer, which is different from the dominant w' for the Fourier mode (0.3, 7) shown in Fig. 8. The evolution of the I indicator of (0.15, 1) indicates the importance of streamwise velocity and temperature perturbations, which reach around 0.6 and 0.2 downstream, respectively.

To evaluate the role of the modal instability around the peak gain in Fig. 10, the PSE analysis is employed. As shown in Fig. 13, the initial transient growth stage is not captured by PSE initialized by mode S. However, in the second-stage growth, a good agreement is reached for both N-factors and fluctuation profiles between resolvent analysis and PSE, which indicates the presence of the unstable oblique first mode evolving from mode S. This comparison confirms the appearance of the first mode with a low frequency and low spanwise wavenumber under the adiabatic wall condition.

Fig. 14 provides the N-factor of the streak, the plane and the oblique optimal disturbances considering three different

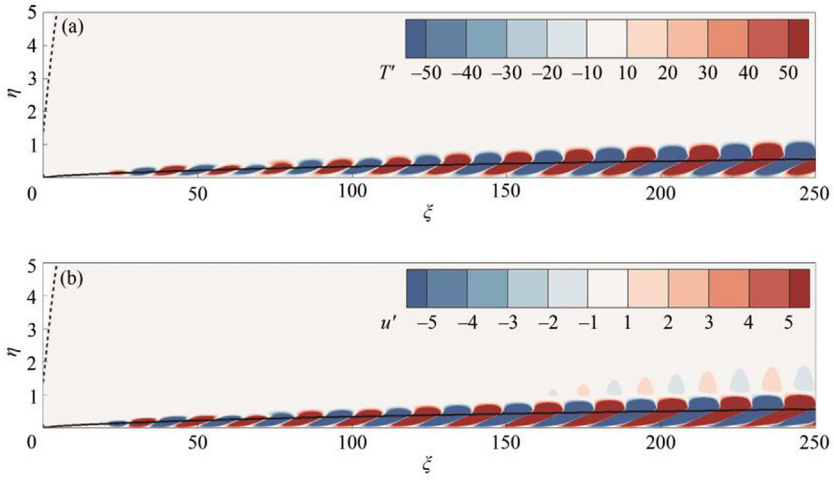

Fig. 11 Contours of normalized (a) temperature and (b) streamwise velocity perturbation components of optimal response for Fourier mode (0.15, 1) under adiabatic wall. The solid and dashed black lines mark the locations of the boundary layer edge and the entropy layer edge, respectively.

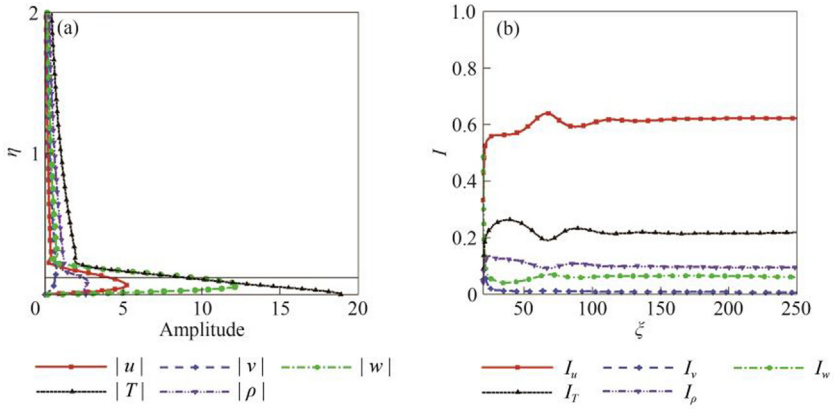

Fig. 12 (a) Input forcing profiles and (b) *I* indicators of Chu energy of optimal response for Fourier mode (0.15, 1) under adiabatic wall.

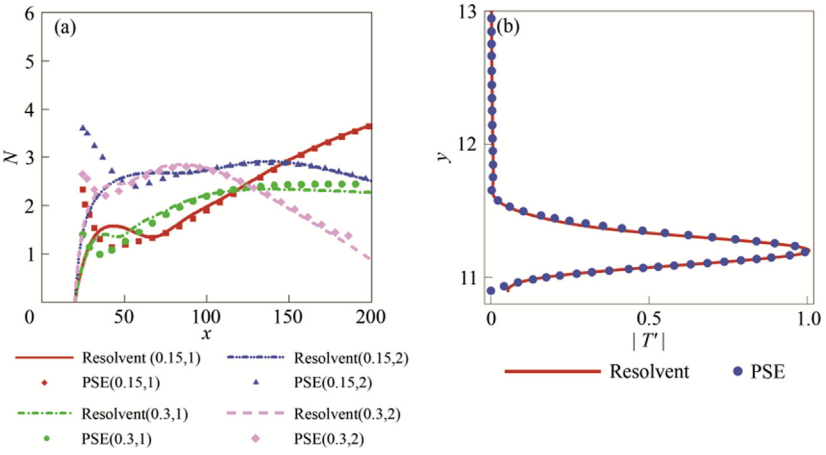

Fig. 13 Comparison of (a) integrated *N*-factors, and (b) fluctuation temperature profiles for (0.15, 1) at $x = 100$ (normalized by its maximal value inside the boundary layer) obtained by PSE and resolvent analysis.

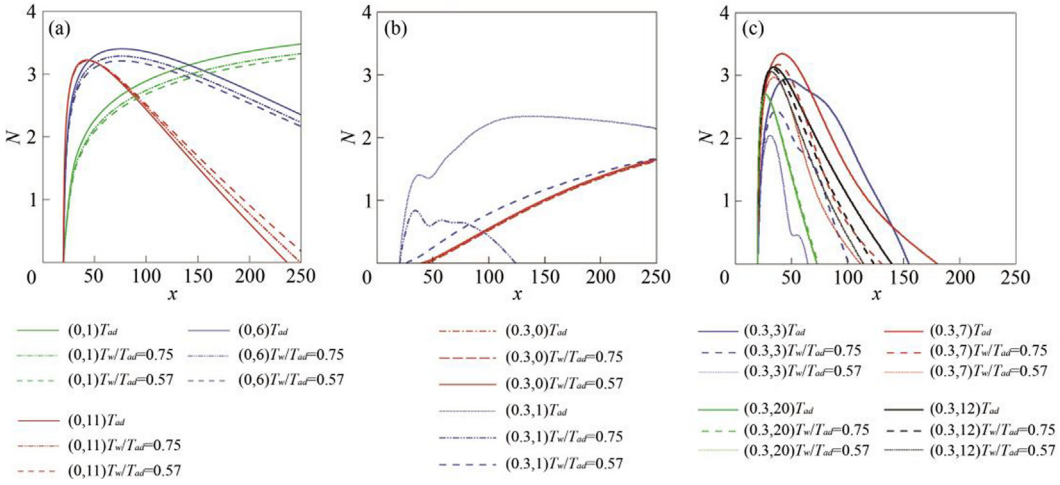

Fig. 14 *N*-factor evolution of (a) streaks, (b) planar and oblique optimal waves with small β, and (c) oblique optimal waves with larger β along x.

wall temperature conditions. Here, cases with a fixed frequency $\omega = 0.3$ (corresponding to 50 kHz) are selected, which correspond to a representative low frequency. It is indicated that wall cooling has nearly no effect on the plane wave while suppressing the transient growth of streaks and oblique waves, especially for lower β. When β increases and exceeds a critical value, the effect of wall temperature becomes minor for both optimal streaks and oblique waves.

The different effects of the wall temperature on the optimal disturbance can be attributed to their different growth patterns, as shown in Section 2. Specifically, the optimal plane wave is mainly distributed in the entropy layer, while the wall cooling effect only changes the mean variables inside the boundary layer, as indicated in Fig. 15. Therefore, wall cooling only affects the optimal oblique waves, which mainly lie inside the boundary layer and contain a pronounced temperature fluctuation. One special case is that the pattern-A response (0.3, 1) is located inside the entropy layer for the baseline cold wall, whereas the response switches to the growth pattern B (oblique wave inside the boundary layer) as the wall temperature increases, as shown in Fig. 14(b). This indicates that the optimal response pattern not only depends on β for a fixed frequency but also may change with other parameters, such as the wall temperature. Consequently, wall cooling may serve as a potential control strategy for pronounced nonmodal disturbances over blunt bodies, which has rarely been mentioned before.

3.4. *Effect of bluntness*

The transition reversal for high-speed flows over blunt bodies was first reported in 1983.[7] However, the physical mechanism behind it remains a debate currently. When the nose radius is approaching the reversal value, the modal instability has been confirmed to be of insufficient significance by linear stability analysis to trigger the transition, including the newly generated inflection instability arising from the entropy layer (entropy layer mode).[11–13,60] However, the nonmodal disturbance inside

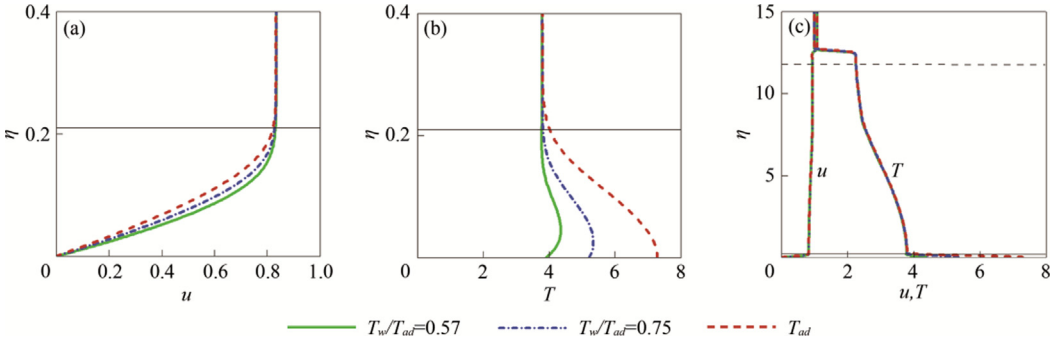

Fig. 15 Mean (a) streamwise velocity and (b) temperature profile distributions near the wall, and (c) mean profiles outside boundary layer at $\xi = 20$. The solid and dashed black lines mark the locations of the boundary layer edge and the entropy layer edge, respectively.

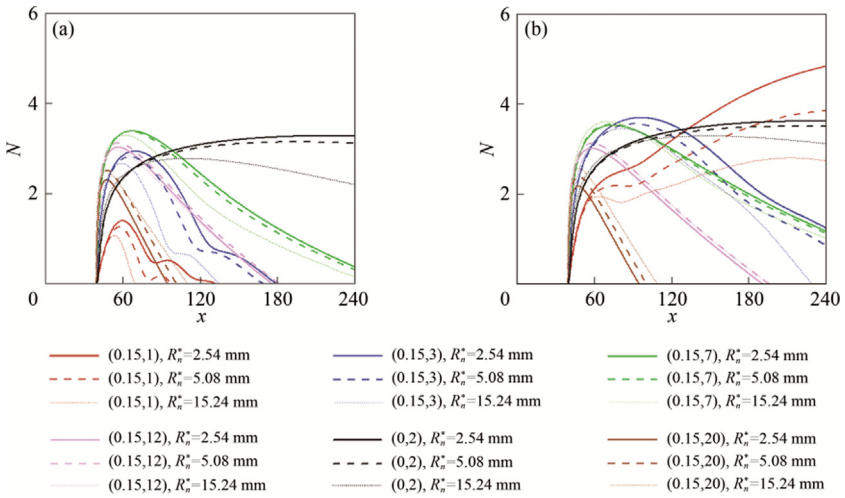

Fig. 16 N-factor distributions of optimal disturbance with different bluntness for (a) $T_w/T_{ad} = 0.57$ and (b) $T_w = T_{ad}$.

the entropy layer has been recognized to be possible to penetrate the boundary layer and excite a strong instability.[9,14,60] Recently, the nonmodal disturbance in the entropy layer has shown an alternative oblique transition route when there is no considerable second modal growth.[21,65] The nonmodal instability, when the nose radius exceeds a certain value, may provide a potential explanation for the transition reversal from the perspective of receptivity and linear instability.

Fig. 16 provides a comparison of the N-factor of low-frequency (e.g., $\omega = 0.15$) optimal oblique waves and stationary streaks with the same ω and β yet different nose radii. The forcing location is fixed at $x = 40$ for all cases. Here, only pattern-B responses are displayed, because pattern-A responses lose their dominance as the increment of bluntness. These pattern-A responses correspond to no positive N-factor in Fig. 16 for $R_n^* = 5.08$ mm and $R_n^* = 15.24$ mm. The unstable first mode (0.15, 1) gets suppressed as the increment of bluntness for both modal instability and transient growth, as shown in Fig. 16(b). For other oblique waves, the suppression effect of bluntness becomes weaker as β increases. Finally, the N factor of oblique waves can be increased with growing bluntness when β exceeds a critical value. However, in the meantime, the N factor is also smaller for a large β. To conclude, increasing bluntness can suppress or strengthen the optimal response, depending on the spanwise wavenumber. Moreover, optimal disturbances obtained by resolvent analysis here exhibit no visible reversal-related phenomenon for a certain combination of ω and β with the increment of bluntness. An expected reversal-related result is that the N-factor increases as the nose radius varies from 2.54 mm to 5.08 mm then decreases as it further rises to 15.24 mm. This observation agrees with the observation by Aswathy Nair and Unnikrishnan,[24] which reported no transition reversal phenomenon when the white noise is initialized downstream of the shock.

The receptivity process provides the initial frequency and amplitude of the optimal responses at the forcing location. Considering this physical process, the effect of nose radii is revisited. The slow acoustic wave is added to the free stream to produce the response of the boundary layer. Note that only a representative single low-frequency ($\omega = 0.15$) forcing is adopted here with the same amplitude for blunt-wedge flows

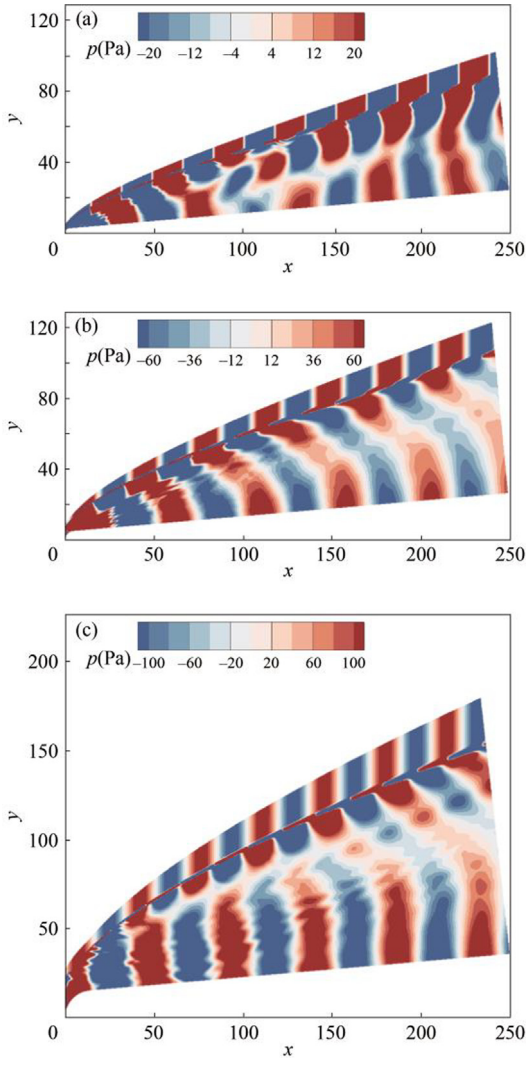

Fig. 17 Contours of instantaneous dimensional pressure fluctuations for (a) $R_n^* = 2.54$ mm, (b) $R_n^* = 5.08$ mm, and (c) $R_n^* = 15.24$ mm.

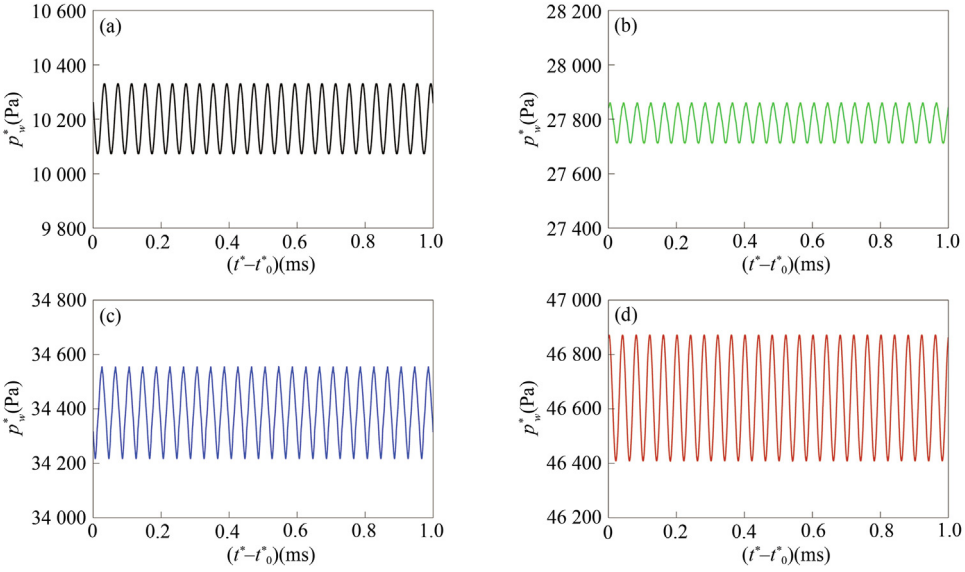

Fig. 18 Instantaneous pressure at (a) free stream and $x = 40$ along the wall for (b) $R_n^* = 2.54$ mm, (c) $R_n^* = 5.08$ mm, and (d) $R_n^* = 15.24$ mm.

with different nose radii. The corresponding physical frequency is 25 kHz, which has shown its significance in the above resolvent analysis. This frequency magnitude also falls within the dominant frequency range of wind-tunnel experiments for blunt cones[15] and Ogive-cylinders.[25] For brevity, only adiabatic wall condition cases are displayed.

As indicated by Fig. 17, the free-stream slow acoustic wave first interacts with the bow shock, and then the resulting disturbance penetrates the entropy layer and excites responses inside the boundary layer. The pressure history in the free stream and on the wall for three blunt wedges is displayed in Fig. 18. Here, t_0^* is the time when the statistical stationary process begins. In terms of the response at the forcing location, the amplitude of the pressure fluctuation at $x = 40$ becomes larger as the increment of nose bluntness. The Root Mean Square (RMS) of pressure at $x = 40$, normalized by its free-stream value, is 0.554, 1.159, and 1.811 for $R_n^* = 2.54$ mm, $R_n^* = 5.08$ mm, and $R_n^* = 15.24$ mm, respectively. This indicates a stronger receptivity process with an increase of nose radius, which may result from a stronger bow shock and thereby intensified shock-disturbance interaction.

With the amplitude of disturbance obtained by the receptivity process, the initial forcing amplitude of optimal disturbances at $x = 40$ is replaced. Fig. 19(a) illustrates the normalized RMS of pressure fluctuations along the wall for different optimal disturbances. Here, the amplitude at $x = 40$ is obtained by the receptivity study, and the further amplitude evolution downstream is obtained from resolvent analysis (see Fig. 17(b)). Subsequently, the two amplitude ratio is multiplied to figure out the final normalized RMS with respect to the freestream value. Physically, Fig. 19(a) suggests the response magnitude under the same level of wind-tunnel noise in real-life situations. Compared with Fig. 17(b), as the increment of bluntness, the strength of the oblique wave (0.15, 7) upstream becomes comparable to the first mode (0.15, 1) downstream. Fig. 19(b) depicts the maximum RMS of pressure fluctuations in the computational domain among all the calculated Fourier modes for different nose radii, which can be seen in Fig. 19(a). The blue line is obtained from a nonlinear fitting procedure to show the data trend. It indicates that as increment of nose radius, the maximized root mean square of pressure decreases and then increases after bluntness exceeds its critical value. The experimental reversal Reynolds number based on the nose radius is around 1×10^6.[16] The resulting critical nose radius is about 10 mm. As a result, a qualitative agreement is reached in the data trend. The above observation may demonstrate the significance of nonmodal disturbances upstream when the modal components are suppressed as the nose radius increases. Specifically, the oblique waves with relatively large spanwise wavenumber show their potential in triggering the transition rather than the suppressed first mode downstream for large bluntness cases. The strengthening of receptivity and transient growth of oblique waves upstream might provide some insights into the transition reversal phenomenon observed in wind-tunnel experiments, which merits further research considering nonlinear-instability and breakdown stages.

This section only provides the evolution of energy magnitude of optimal disturbances over the blunt wedge from a small to large nose radius. The parametric study may benefit a further investigation to fully understand the reason for the transition reversal phenomenon using a three-dimensional simulation of the complete stage.

3.5. Orr/lift up mechanism analysis

In this Section, two classical mechanisms of transient growth, i.e., Orr and lift-up mechanisms, are analyzed. Disturbances

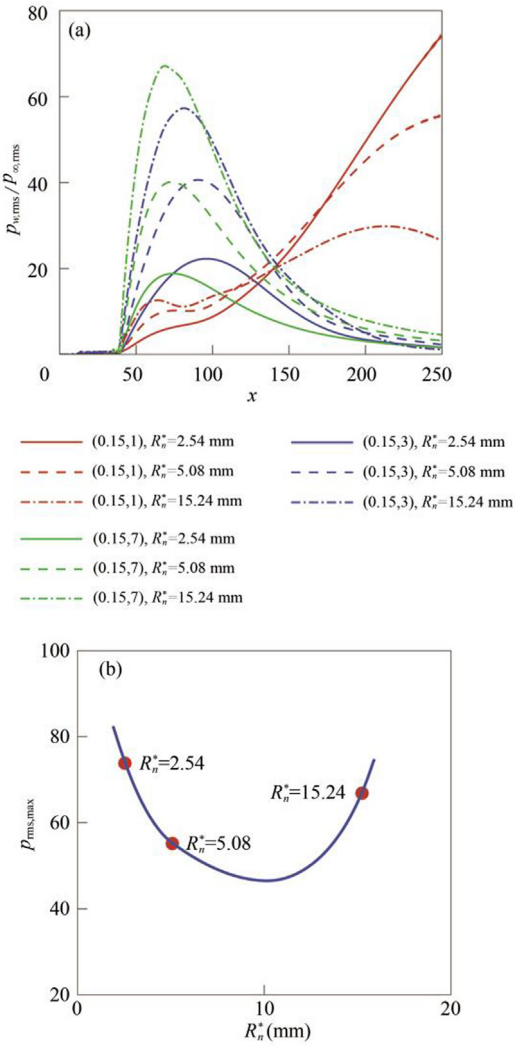

Fig. 19 (a) The normalized root mean square of pressure along the wall, and (b) the maximize root mean square of pressure fluctuations in the computational domain among all the calculated Fourier modes for different blunt wedges. Line in (b) represents the data trend from fitting. The experimental reversal nose-tip radius is about 10 mm.

are amplified by Orr mechanism when they have streamlines tilted against the mean shear and become stronger when the base flow reorients them.[66] The lift-up effect arises when streamwise vortices form streaky structures by displacing fluid particles in the wall-normal direction, which maintains their horizontal momentum.[67] To quantify the intensity of the vorticity transfer, the streamwise evolution of the integrated enstrophy ratios[68,69] is analyzed, which is characterized by

$$\begin{cases} r_l(x) = \Omega_l / \sum_i \Omega_i \\ \Omega_i(x) = \int_0^\infty \varpi_i^2 \mathrm{d}y \\ i = x, y, z; l = 1, 2, 3 \end{cases} \tag{16}$$

where ϖ_x, ϖ_y, and ϖ_z represent the streamwise, wall-normal, and spanwise vorticity, respectively. Fig. 20 gives the integrated enstrophy ratio for some representative combinations of ω and β. Overall, these combinations show the same trend: the decrease of streamwise vorticity components and the increase of spanwise vorticity. Note that the transfer of vorticity from the streamwise direction to the spanwise direction is associated with the lift-up mechanism. Among them, pattern-B disturbances (0.3, 7) and (0, 2) nearly collapse onto the same curve, which probably indicates that (0.3, 7) shares the characteristics of unsteady streaks. Interestingly, the vorticity transfer of the pattern-A wave (0.45, 1) is weaker than the other optimal disturbances, which is characterized by a tardy vorticity transfer near the forcing location. This indicates that pattern-B responses possess a more efficient lift-up mechanism than pattern-A responses, which can also be seen in Appendix B.

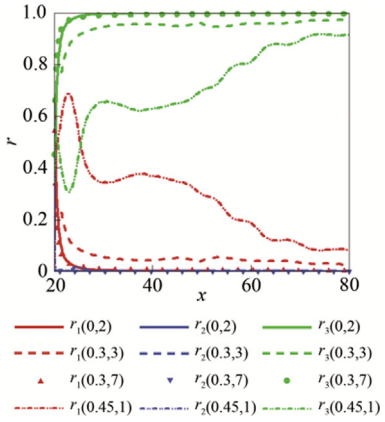

Fig. 20 Evolution of enstrophy ratios for Fourier modes (0, 2), (0.3, 3), and (0.3, 7).

Fig. 21 depicts the streamwise, wall-normal, and spanwise vorticity components of the optimal pattern-A wave (0.45, 1). The gradual change of the vorticity orientation indicates the existence of the Orr mechanism, where tilted vortices extract energy from the mean flow while being erected.[46,70] For incompressible flows, nonmodal growth due to the Orr mechanism is ascribed to the extraction of energy from the mean shear by conveying momentum along the mean momentum gradient via the Reynolds shear stress.[71,72] However, the energy amplification observed in this hypersonic scenario is primarily due to the temperature gradient within the entropy layer. As illustrated in Fig. 15(c), the characteristic of the hypersonic blunt wedge flow is that the mean temperature gradient is substantially more prominent than the streamwise velocity gradient. Thus, the interaction between the disturbance and the mean flow via the Reynolds thermal stress in the entropy layer appears to be significant for the Orr mechanism.

Individual energy contribution analysis is then performed to characterize the effect of wall temperature on the optimal disturbance. As shown in Fig. 22, reducing wall temperature would lead to a more substantial streamwise velocity disturbance component and weaker temperature and density components. This suggests that when wall cooling is applied, the thermodynamic part of energy becomes less significant com-

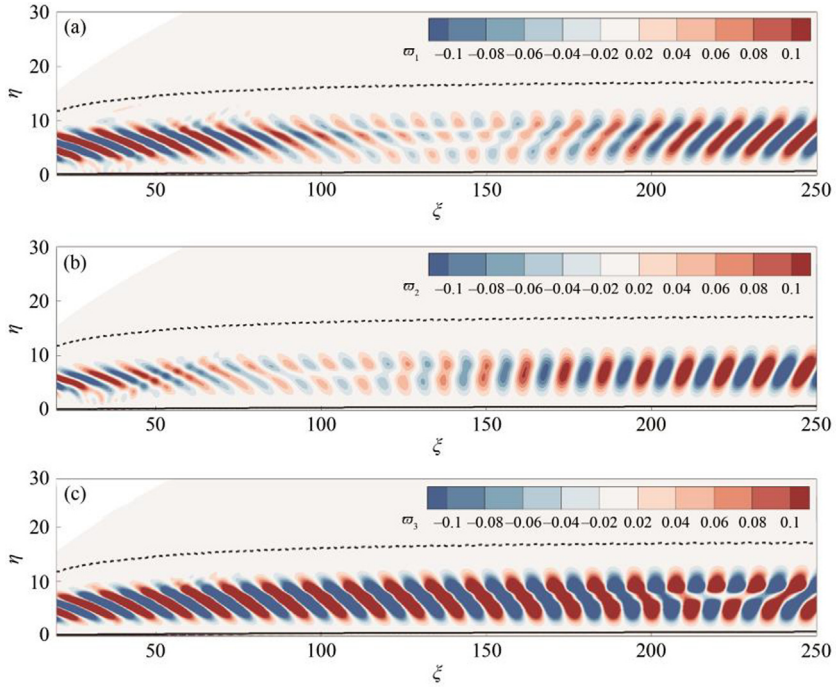

Fig. 21 Contours of (a) streamwise, (b) wall-normal, and (c) spanwise vorticity of the pattern-A response (0.45, 1). The solids and dashed black lines mark the locations of the boundary layer edge and the entropy layer edge, respectively.

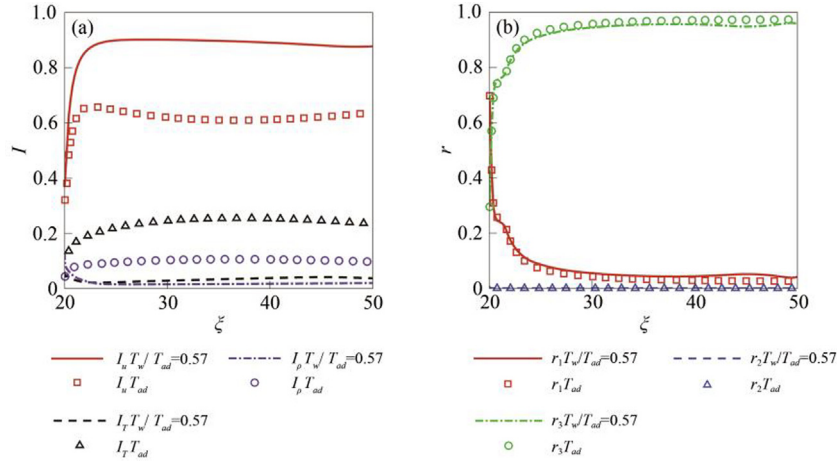

Fig. 22 (a) I indicators of Chu energy and (b) enstrophy ratios of pattern-B response (0.3, 3).

pared to the kinetic part. These may be associated with the modified mean flow gradient inside the boundary layer. The adiabatic wall condition results in a steeper temperature gradient, which in turn strengthens thermodynamic fluctuations components and eventually leads to a stronger Pattern-B wave. As for the enstrophy ratios, wall cooling almost does not affect the evolution of their values. This indicates that the vorticity transfer process is weakly affected by the wall temperature. The same curve and conclusion can be obtained for streaks, not shown here for brevity.

4. Conclusions

In this work, resolvent analysis is utilized to study the optimal disturbance of the hypersonic flow over a blunt wedge at Mach number 5.9 and a unit Reynolds number of 91.5×10^6/m. With the absence of the second-mode disturbance, the low-frequency (within 50 kHz) associated modal and nonmodal disturbances are identified and examined with the parabolic stability equation analysis. The growth pattern of optimal disturbances is investigated with consideration of the effects of

wall temperature (T_w/T_{ad} = 0.57, T_w/T_{ad} = 0.75, and adiabatic wall) and nose radius (R_n* = 2.54, 5.08, and 15.24 mm). The lift-up/Orr transient growth mechanisms sustaining the nonmodal amplification of the optimal response are also studied. The main conclusion is summarized as follows:

(1) For a fixed frequency, with the increment of the spanwise wavenumber, competitive patterns of optimal disturbances are identified. This competition is due to the appearance of nearly equally significant optimal and sub-optimal solutions. Specifically, the optimal response of the system is firstly shown as disturbances propagating inside the entropy layer (pattern A), and then switches to the pattern inside the boundary layer (pattern B). The former pattern A experiences a long-distance energy growth, while the latter pattern B undergoes a rapid transient growth followed by a significant decay. The significant decay can be interpreted as the steady oblique mode S when the spanwise wave number is not larger than 5 in the studied cases.
(2) Compared to the baseline cold wall condition (T_w/T_{ad} = 0.57), the adiabatic wall condition supports the appearance of the unstable oblique first mode. The optimal oblique wave first experiences a rapid transient growth and then a modal growth, resulting in a higher N-factor than other kinds of disturbances, including streaks. Moreover, the cold wall condition tends to weaken the transient growth of oblique waves inside the boundary layers (pattern B), especially for low-spanwise-wavenumber cases. For optimal patterns travelling inside the entropy layer (pattern A), the effect exerts no influence since the base flow inside the entropy layer is hardly affected by the wall temperature.
(3) Regarding the influence of the nose radius, the resolvent analysis shows no discernible improvement in an understanding of either modal or nonmodal growth. Nonetheless, considering the receptivity to the slow acoustic wave, the amplitude of nonmodal oblique waves within the boundary layer increases with the nose bluntness. The enhanced nonmodal oblique wave in the upstream region approaches that of the first mode downstream. The strengthened receptivity of oblique waves with relatively large spanwise wavenumber (say, β = 7 for R_n* = 15.24 mm) may potentially cause the transition to move upstream. An estimated amplitude response favorably reproduces the reversal-like phenomenon. A three-dimensional simulation of the complete stage (from receptivity to transition) is expected in the future.
(4) Both Orr and lift-up mechanisms play a significant role in the transient growth of optimal disturbances. This deduction particularly holds true for pattern-A optimal responses, which are manifested as tilted waves inside the entropy layer. The Orr mechanism is more likely to be accomplished by energy transfer via the mean temperature gradient rather than the mean shear. This is because the base velocity gradient in the entropy layer is ignorable compared to the temperature gradient. Furthermore, pattern-B responses possess a more efficient lift-up mechanism than pattern-A responses according to an enstrophy ratio criterion.

The base flow is limited to two-dimensional cases in this study, and the linear assumption is applied to disturbance equations. Furthermore, the resolvent analysis only yields the optimal disturbances that experience the largest energy gain in the studied computational domains, which serve as the upper boundary or the most dangerous scenario subject to external forcings. It may not be realisable by wind-tunnel experiments under specific environments. In the future, the role of these disturbances of various patterns should be adequately considered in the Fourier space for a transitional hypersonic flow over blunt bodies. The corresponding transition to turbulence under the realistic wind tunnel condition with broadband noise may be a combinational consequence of various kinds of disturbance which are selected to be considerably amplified.

CRediT authorship contribution statement

Yifeng CHEN: Writing – original draft, Visualization, Investigation, Data curation. **Tianju MA:** Supervision, Resources, Conceptualization. **Peixu GUO:** Writing – review & editing, Supervision, Project administration, Conceptualization. **Jiaao HAO:** Writing – review & editing, Software, Resources, Conceptualization. **Chihyung WEN:** Writing – review & editing, Supervision.

Declaration of competing interest

The authors declare that they have no known competing financial interests or personal relationships that could have appeared to influence the work reported in this paper.

Acknowledgements

This work was supported by the Hong Kong Research Grants Council (Nos. 15216621, 15204322, 25203721) and the National Natural Science Foundation of China (No. 12102377).

Appendix A. Verification of grid independence

Computational grids are constructed with two different grid resolutions, including 750 × 300 (coarse) and 1000 × 400 (fine) in the streamwise and wall-normal directions, respectively. Note that the grid near the wall and the bow shock are clustered. Here, only is the case for R_n* = 2.54 mm and T_w/T_{ad} = 0.57 shown for brevity. The same conclusion can be obtained for other cases. Fig. A1 compares the mean temperature contour between the coarse and fine grids, and Fig. A2 compares the N-factor distribution of representative optimal responses for two sets of grids. It is indicated that the coarse grid is sufficient for both the base-flow simulation and the resolvent analysis for the frequency of interest in this study.

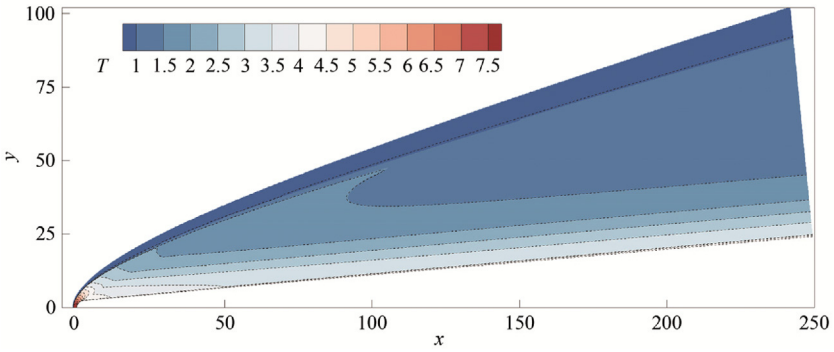

Fig. A1 Contour of mean temperature of fine grid (contour) and coarse grid (dashed line) for $R_n^* = 2.54$ mm and $T_w/T_{ad} = 0.57$.

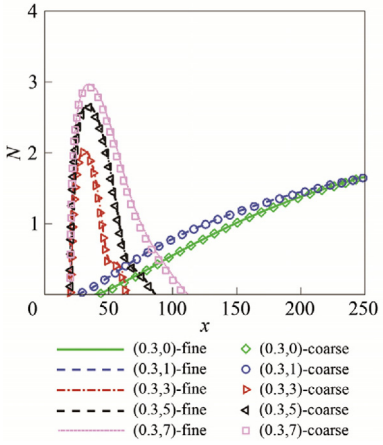

Fig. A2 Evolution of N-factor of representative optimal responses for $R_n^* = 2.54$ mm and $T_w/T_{ad} = 0.57$.

Appendix B. Competitive patterns of optimal and sub-optimal disturbances

The optimal disturbance can be viewed as an upper bound of the response of the system, while realistic external disruptions typically lead to a suboptimal transient growth. As shown in Fig. B1, the optimal response switches from pattern A to pattern B as β increases, the competition between these two patterns can be revealed by extracting both the optimal and sub-optimal responses. The sub-optimal disturbance can be captured using an Arnoldi iteration to search for more eigenvalues. Here, we display the optimal (pattern-B family) and sub-optimal (pattern-A family) disturbances for the Fourier mode (0.3, 2). This mode is typical to facilitate an understanding of the competition between different patterns.

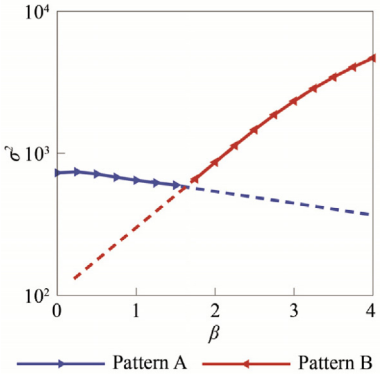

Fig. B1 Optimal gain (solid line) along spanwise wavenumber β for $\omega = 0.3$. Dashed lines indicate the extension of solid lines.

As shown in Fig. B2(a), the optimal response demonstrates a rapid growth near the forcing location, while the other non-optimal disturbances experience a gradual growth downstream. Note that the optimal gain decreases monotonically from the optimal response to the first, second, third, and fourth sub-optimal responses. According to Fig. B2(b), the vorticity transfer from the streamwise direction to the spanwise direction is more efficient for optimal disturbances, followed by the first, second, third, and fourth sub-optimal responses. This is because the optimal response achieves a rapid r_1-dominated state downstream of the forcing location. Therefore, the lift-up mechanism may play a significant role in the competition between optimal and relevant sub-optimal disturbances.

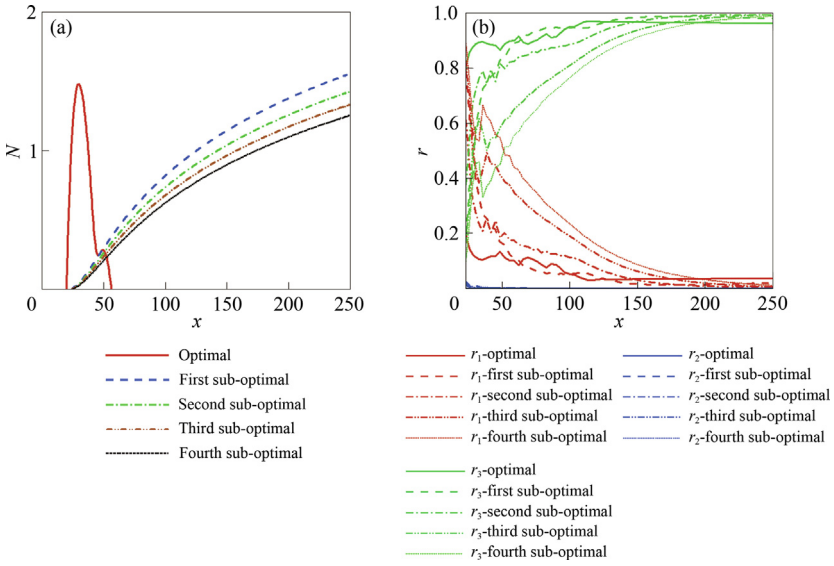

Fig. B2 Evolution of (a) *N*-factor and (b) enstrophy ratios of optimal and the first, second, third and fourth sub-optimal responses for Fourier mode (0.3, 2).

The temperature fluctuation contours for optimal and four sub-optimal disturbances for (0.3, 2) are shown in Fig. B3. The optimal disturbance is distributed inside the boundary layer, while the sub-optimal disturbances show their signature inside the entropy layer. The non-optimal disturbances present a tilting structure that seems to be associated with the Orr mechanism. The disturbances inside the entropy layer may be related to the wisp-like structures observed in the wind-tunnel experiment when the first and second modes are not dominant.[23,25] The nonlinear evolution and potential transition process induced by these disturbances merits further investigation.

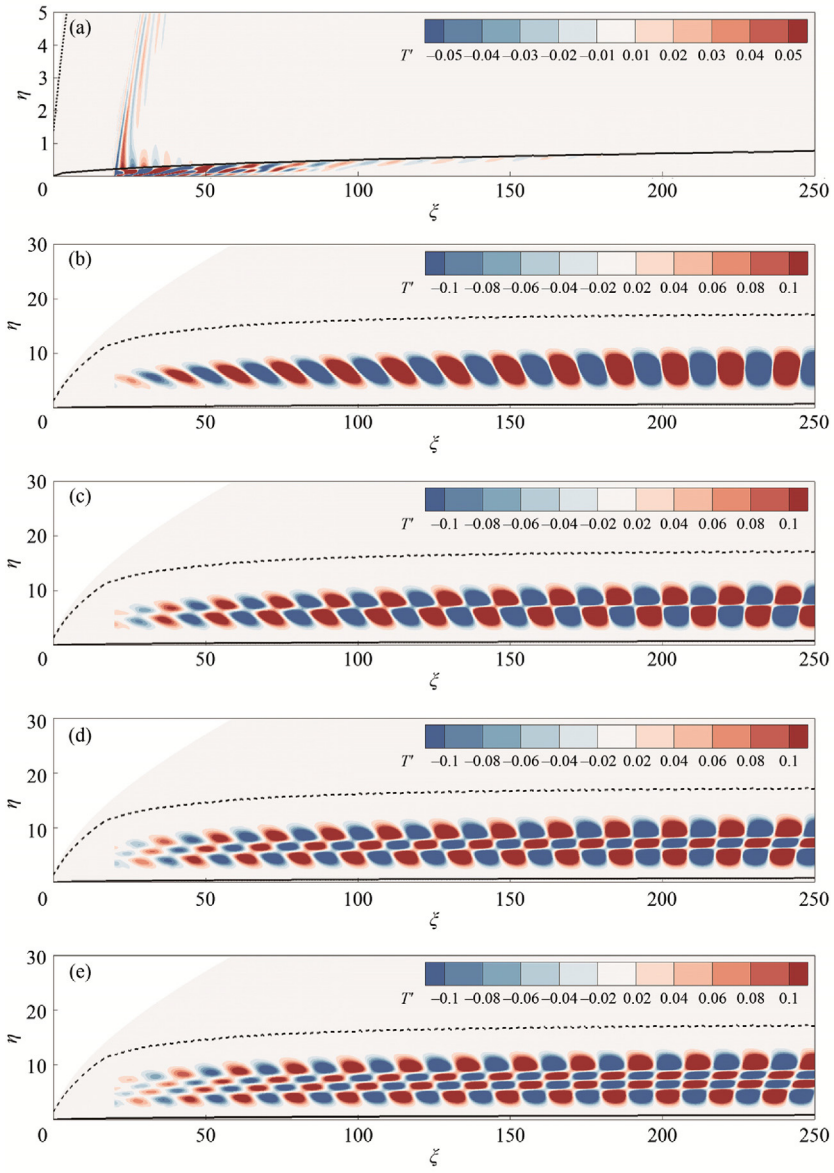

Fig. B3 Contours of normalized temperature fluctuations for (a) optimal response and the (b) first, (c) second, (d) third and (e) fourth sub-optimal responses for (0.3, 2). The solid and dashed black lines mark the locations of the boundary layer edge and the entropy layer edge, respectively.

References

1. Chen JQ, Tu GH, Zhang YF, et al. Hypersnonic boundary layer transition: What we know, where shall we go. *Acta Aerodynamica Sinica* 2017;**35**(3):311–37 [Chinese].
2. Mack L. Boundary-layer linear stability theory. *AGARD special course on stability and transition of laminar flow*. 1984.
3. Fedorov AV. Receptivity of a high-speed boundary layer to acoustic disturbances. *J Fluid Mech* 2003;**491**:101–29.
4. Ma YB, Zhong XL. Receptivity of a supersonic boundary layer over a flat plate. Part 1. Wave structures and interactions. *J Fluid Mech* 2003;**488**:31–78.
5. Chen JQ, Yi SH, Li XL, et al. Theoretical, numerical and experimental study of hypersonic boundary layer transition: Blunt circular cone. *Appl Therm Eng* 2021;**194**:116931.
6. Zhou JT, Cao W. Effects of entropy layer on the boundary layer over hypersonic blunt cones considering entropy swallowing. *Phys Fluids* 2021;**33**(7):034111.
7. Stetson K. Nosetip bluntness effects on cone frustum boundary layer transition in hypersonic flow. *16th fluid and plasmadynamics conference*; Danvers, MA. Reston: AIAA; 1983.
8. Wan BB, Chen JQ, Tu GH, et al. Effects of nose bluntness on entropy-layer stabilities over cones and wedges. *Acta Mechanica Sinica* 2022;**39**(1):122176.
9. Ba WT, Niu MH, Su CH. Hypersonic boundary-layer receptivity over circular cones with ellipsoidal/spherical noses. *AIAA J* 2022;**61**(2):518–33.
10. Rushton GH, Stetson KF. Shock tunnel investigation of boundary-layer transition at M equals 5.5. *AIAA J* 1967;**5**(5):899–906.
11. Dietz G, Hein S. Entropy-layer instabilities over a blunted flat plate in supersonic flow. *Phys Fluids* 1999;**11**(1):7–9.
12. Fedorov A, Tumin A. Evolution of disturbances in entropy layer on a blunted plate in supersonic flow. *32nd AIAA fluid dynamics conference and exhibit*; St. Louis, Missouri. Reston: AIAA; 2002.
13. Wan BB, Luo JS, Su CH. Response of a hypersonic blunt cone boundary layer to slow acoustic waves with assessment of various routes of receptivity. *Appl Math Mech* 2018;**39**(11):1643–60.
14. Wan BB, Su CH, Chen JQ. Receptivity of a hypersonic blunt cone: Role of disturbances in entropy layer. *AIAA J* 2020;**58**(9):4047–54.
15. Paredes P, Choudhari MM, Li F, et al. Nose-tip bluntness effects on transition at hypersonic speeds. *J Spacecr Rockets* 2018;**56**(2):369–87.
16. Paredes P, Choudhari MM, Li F. Blunt-body paradox and transient growth on a hypersonic spherical forebody. *Phys Rev Fluids* 2017;**2**(5):053903.
17. Paredes P, Choudhari MM, Li F, et al. Nonmodal growth of traveling waves on blunt cones at hypersonic speeds. *AIAA J* 2019;**57**(11):4738–49.
18. Paredes P, Choudhari MM, Li F, et al. Nosetip bluntness effects on transition at hypersonic speeds: Experimental and numerical analysis under nato sto avt-240. *2018 AIAA aerospace sciences meeting*; Kissimmee, Florida. Reston: AIAA; 2018.
19. Paredes P, Choudhari MM, Li F. Blunt-body paradox and improved application of transient-growth framework. *AIAA J* 2018;**56**(7):2604–14.
20. Paredes P, Choudhari MM, Li F, et al. Optimal growth in hypersonic boundary layers. *AIAA J* 2016;**54**(10):3050–61.
21. Hartman AB, Hader C, Fasel HF. Nonlinear transition mechanism on a blunt cone at Mach 6: Oblique breakdown. *J Fluid Mech* 2021;**915**:R2.
22. Kennedy RE, Jagde EK, Laurence SJ, et al. Visualizations of hypersonic boundary-layer transition on a variable bluntness cone. *AIAA aviation 2019 forum*; Dallas, Texas. Reston: AIAA; 2019.
23. Kennedy RE, Jewell JS, Paredes P, et al. Characterization of instability mechanisms on sharp and blunt slender cones at Mach 6. *J Fluid Mech* 2022;**936**:A39.
24. Aswathy Nair K, Unnikrishnan S. Effects of nose bluntness on hypersonic transition over ogive-cylinder forebodies. *AIAA J* 2023;**62**(2):476–88.
25. Hill JL, Oddo RA, Komives JR, et al. Experimental measurements of hypersonic instabilities over ogive-cylinders at Mach 6. *AIAA J* 2022;**60**(8):4492–508.
26. Scholten A, Paredes P, Luke Hill J, et al. Linear instabilities over ogive-cylinder models at Mach 6. *AIAA J* 2022;**60**(8):4478–91.
27. Goparaju H, Unnikrishnan S, Gaitonde DV. Effects of nose bluntness on hypersonic boundary-layer receptivity and stability. *J Spacecr Rockets* 2021;**58**(3):668–84.
28. Duan L, Choudhari MM, Zhang C. Pressure fluctuations induced by a hypersonic turbulent boundary layer. *J Fluid Mech* 2016;**804**:578–607.
29. Laufer J. Aerodynamic noise in supersonic wind tunnels. *J Aerosp Sci* 1961;**28**(9):685–92.
30. Laufer J. Some statistical properties of the pressure field radiated by a turbulent boundary layer. *Phys Fluids* 1964;**7**(8):1191–7.
31. Schneider SP. Effects of high-speed tunnel noise on laminar-turbulent transition. *J Spacecr Rockets* 2001;**38**(3):323–33.
32. Schneider SP. Development of hypersonic quiet tunnels. *J Spacecr Rockets* 2008;**45**(4):641–64.
33. Balakumar P, King RA, Chou A, et al. Receptivity and forced response to acoustic disturbances in high-speed boundary layers. *AIAA J* 2017;**56**(2):510–23.
34. Su CH, Zhou H. Transition prediction of a hypersonic boundary layer over a cone at small angle of attack—with the improvement of eNmethod. *Sci China Ser G Phys Mech Astron* 2009;**52**(1):115–23.
35. Su CH, Zhou H. Transition prediction of the supersonic boundary layer on a cone under the consideration of receptivity to slow acoustic waves. *Sci China Phys Mech Astron* 2011;**54**(10):1875.
36. Zhao R, Liu T, Wen CY, et al. Theoretical modeling and optimization of porous coating for hypersonic laminar flow control. *AIAA J* 2018;**56**(8):2942–6.
37. Zhao R, Wen C, Zhou Y, et al. Review of acoustic metasurfaces for hypersonic boundary layer stabilization. *Prog Aerosp Sci* 2022;**130**:100808.
38. Zhao R, Wen CY, Long TH, et al. Spatial direct numerical simulation of the hypersonic boundary-layer stabilization using porous coatings. *AIAA J* 2019;**57**(11):5061–5.
39. Guo PX, Liu X, Zhao R, et al. Effect of acoustic metasurface on hypersonic-boundary-layer wave packet. *Phys Fluids* 2023;**35**(9):094110.
40. Masad JA, Abid R. On transition in supersonic and hypersonic boundary layers. *Int J Eng Sci* 1995;**33**(13):1893–919.
41. Mack LM. On the inviscid acoustic-mode instability of supersonic shear flows. *Theor Comput Fluid Dyn* 1990;**2**(2):97–123.
42. Fedorov A. Transition and stability of high-speed boundary layers. *Annu Rev Fluid Mech* 2011;**43**:79–95.
43. Chen YF, Guo PX, Wen C. A unified explanation of energy growth sources for unstable modes in flat-plate boundary layers. *J Fluid Mech* 2023;**972**:A5.
44. Zhou T, Lu YH, Yan C. Investigation of influence of local cooling/heating on nonlinear instability of high-speed boundary layer with direct numerical simulations. *Chin J Aeronaut* 2023;**36**(12):77–87.
45. Nie H, Song WP, Han ZH, et al. Attenuation of boundary-layer instabilities for natural laminar flow design on supersonic highly swept wings. *Chin J Aeronaut* 2024;**37**(11):118–37.
46. Tempelmann D, Hanifi A, Henningson DS. Spatial optimal growth in three-dimensional compressible boundary layers. *J Fluid Mech* 2012;**704**:251–79.

47. Tumin A, Reshotko E. Optimal disturbances in compressible boundary layers. *AIAA J* 2003;**41**(12):2357–63.
48. Tumin A, Reshotko E. Optimal disturbances in the boundary layer over a sphere. *Proceedings of the 34th AIAA fluid dynamics conference and exhibit*; Portland, Oregon. Reston: AIAA; 2004.
49. Jewell JS, Kennedy RE, Laurence SJ, et al. Transition on a variable bluntness 7-degree cone at high Reynolds number. *2018 AIAA aerospace sciences meeting*; Kissimmee, Florida. Reston: AIAA; 2018.
50. Guo PX, Hao JA, Wen CY. Interaction and breakdown induced by multiple optimal disturbances in hypersonic boundary layer. *J Fluid Mech* 2023;**974**:A50.
51. Hao JA, Cao SB, Guo PX, et al. Response of hypersonic compression corner flow to upstream disturbances. *J Fluid Mech* 2023;**964**:A25.
52. Hao JA, Cao SB, Wen CY, et al. Occurrence of global instability in hypersonic compression corner flow. *J Fluid Mech* 2021;**919**:A4.
53. Hao JA, Wen CY. Hypersonic flow over spherically blunted double cones. *J Fluid Mech* 2020;**896**:A26.
54. Cao SB, Hao JA, Guo PX, et al. Stability of hypersonic flow over a curved compression ramp. *J Fluid Mech* 2023;**957**:A8.
55. Chu BT, Kovasznay LSG. Non-linear interactions in a viscous heat-conducting compressible gas. *J Fluid Mech* 1957;**3**:494–514.
56. Bugeat B, Chassaing JC, Robinet JC, et al. 3D global optimal forcing and response of the supersonic boundary layer. *J Comput Phys* 2019;**398**:108888.
57. Guo PX, Gao ZX, Jiang CW, et al. Linear stability analysis on the most unstable frequencies of supersonic flat-plate boundary layers. *Comput Fluids* 2020;**197**:104394.
58. Guo PX, Gao ZX, Jiang CW, et al. Sensitivity analysis on supersonic-boundary-layer stability subject to perturbation of flow parameters. *Phys Fluids* 2021;**33**(8):084111.
59. Guo PX, Shi FC, Gao ZX, et al. Sensitivity analysis on supersonic-boundary-layer stability: Parametric influence, optimization, and inverse design. *Phys Fluids* 2022;**34**(10):104113.
60. Chen YF, Tu GH, Wan BB, et al. Receptivity of a hypersonic flow over a blunt wedge to a slow acoustic wave. *Phys Fluids* 2021;**33**(8):084114.
61. Kara K, Balakumar P, Kandil O. Receptivity of hypersonic boundary layers due to acoustic disturbances over blunt cone. *Proceedings of the 45th AIAA aerospace sciences meeting and exhibit*; Reno, Nevada. Reston: AIAA; 2007.
62. Duan L, Choudhari MM, Chou A, et al. Characterization of freestream disturbances in conventional hypersonic wind tunnels. *J Spacecr Rockets* 2018;**56**(2):357–68.
63. Alizard F, Gibis T, Selent B, et al. Stochastic receptivity of laminar compressible boundary layers: An input-output analysis. *Phys Rev Fluids* 2022;**7**(7):073902.
64. Ran W, Zare A, Philipp Hack MJ, et al. Stochastic receptivity analysis of boundary layer flow. *Phys Rev Fluids* 2019;**4**(9):093901.
65. Paredes P, Choudhari MM, Li F. Mechanism for frustum transition over blunt cones at hypersonic speeds. *J Fluid Mech* 2020;**894**:A22.
66. Farrell B. Developing disturbances in shear. *J Atmos Sci* 1987;**44**(16):2191–9.
67. Landahl MT. A note on an algebraic instability of inviscid parallel shear flows. *J Fluid Mech* 1980;**98**:243–51.
68. Alizard F, Pirozzoli S, Bernardini M, et al. Optimal transient growth in compressible turbulent boundary layers. *J Fluid Mech* 2015;**770**:124–55.
69. Guégan A, Huerre P, Schmid PJ. Optimal disturbances in swept Hiemenz flow. *J Fluid Mech* 2007;**578**:223.
70. Orr WMF. The stability or instability of the steady motions of a perfect liquid and of a viscous liquid. Part II: A viscous liquid. *Proc r Irish Acad Sect A: Math Phys Sci* 1907;**27**:69–138.
71. Butler KM, Farrell BF. Three-dimensional optimal perturbations in viscous shear flow. *Phys Fluids* 1992;**4**(8):1637–50.
72. Schmid PJ. Nonmodal stability theory. *Annu Rev Fluid Mech* 2007;**39**:129–62.